Journal of Sound and Vibration (2000) **230**(4), 761–789
doi:10.1006/jsvi.1999.2659, available online at http://www.idealibrary.com on IDEAL®

ADAPTIVE CONTROL OF AEROACOUSTIC INSTABILITIES

M. METTENLEITER, E. HAILE AND S. CANDEL
EM2C Lab., CNRS, Ecole Centrale Paris, 92295 *Châtenay–Malabry Cedex, France*

(*Received* 23 *April* 1999, *and in final form* 10 *September* 1999)

This paper describes an experimental investigation of adaptive control algorithms applied to aeroacoustic instabilities. The study is carried out on a cold flow experimental rig, designed to reproduce the essential features of acoustically coupled vortex shedding. This mechanism is the source of thrust oscillations in large segmented solid rocket motors. It is also found in a wide variety of combustion instabilities. Two adaptive control strategies are investigated and selected experimental results are reported. These results show the feasibility of control. The effect of the controller on the instability mechanism is analyzed and improvements to the control strategy are proposed.

1. INTRODUCTION

Propulsion systems often feature large-amplitude oscillations, or instabilities, which are generally related to acoustically coupled unsteady combustion. The problem may be particularly serious in the case of large volumetric heat release devices. It is also encountered in many practical combustors operating in the lean pre-mixed pre-vaporized mode. Low-frequency thrust oscillations are observed in segmented solid rocket motors (SRMs) which may perturb the flight and increase the vibro-acoustic level in the payload bay. Many possible instability mechanisms exist which achieve the unstable feedback between heat release and acoustic pressure. One such mechanism frequently encountered in practical applications, is unsteady vortex shedding behind dump planes or flow restrictors.

In dump combustors, it has been shown that periodic shedding of vortices, entraining reactants, leads to unsteady heat release when the vortex core ignites or when the vortex breaks down through interactions with neighbouring vortices or the combustion chamber walls. Even in the absence of unsteady heat release in the vortices, the periodic interaction of organized structures with choked exhaust nozzles generates strong acoustic pressure oscillations which may then cause unsteady reactant burning. Such a mechanism may be responsible for the thrust oscillations observed in large segmented solid rocket motors.

Among the possible solutions to such problems, active control has great potential but requires further research before it can be applied in practice. This paper addresses the issue of control algorithms, which is a key point in this

0022-460X/00/090761 + 29 $35.00/0

research. Adaptive techniques are specifically investigated to examine their operational applicability. Using a cold-flow experiment simulating the vortex-shedding instabilities of solid rocket motors, the dynamics of the controller and the controlled system are studied. The experimental configuration is sufficiently generic so that conclusions reached in this case may be extended to other studies of technological interest, where coupling through acoustically triggered vortex shedding plays a role.

The following sections briefly summarize current understanding in the area of solid rocket motor instabilities and identify some of the major questions raised by the application of active control. The experimental configuration, the response of the device, and the adaptive control strategy are then described. Selected experimental results are finally discussed.

2. AEROACOUSTIC INSTABILITIES IN SOLID ROCKET MOTORS

Among the different mechanisms which may drive pressure oscillations in segmented solid rockets, one of the possible sources for the instabilities is the coupling between the longitudinal chamber acoustic modes and vortex shedding from inhibitors protruding into the internal flow (see, for example, Vuillot [1] or Dotson *et al.* [2]).

Experiments with a simplified geometry, where cold gas flows in a duct and passes through a pair of baffles (see Nomoto and Culick [3]), or a pair of diaphragms (see Culick and Magiawala [4] and Dunlap and Brown [5]) support this theory: peaks in pressure transducer spectra close to the acoustic modes are measured in this geometry. It is believed that combustion plays a minor role and that the driving source is essentially aeroacoustic. It may be possible to attenuate pressure oscillations by actively controlling vortex shedding. This may be investigated in a simple laboratory experiment.

Leaving aside many technological aspects (sensors, actuators, etc.) it is important to examine the central issue of control. Adaptive methods are considered specifically to see if they are applicable to aeroacoustic instabilities. The following questions deserve attention:

- Is it possible to control aeroacoustic coupling?
- What is the optimal actuator/sensor combination?
- How much energy is needed to suppress the instability?
- What kind of control algorithms need to be used?

The aim of this paper is to address some of these questions and to gain insight into the complex problem of active control of instabilities.

In the area of fluid mechanics, active feedback control of flow instabilities is now extensively investigated. However, a review of literature indicates that:

- Few studies deal with unstable flows coupled by acoustic (see, for example, Huang and Weaver [6] and Billoud *et al.* [7]) or mechanical (see Huang and Weaver [8]) resonances.

- A limited number of studies consider adaptive control algorithms in the area of unstable flows (see, for example, Billoud *et al.* [7] or Ziada [9]). The disadvantage of non-adaptive algorithms in this context is the necessity to change the controller gain and phase with changing flow speed (see, for example, Ziada [9], Huang and Weaver [6, 8], Ffowcs Williams and Zhao [10], Welsh *et al.* [11] among others).

This work treats adaptive control algorithms applied to unstable flows, coupled with system acoustics.

3. EXPERIMENTAL SET-UP AND PHENOMENA

3.1. EXPERIMENTAL DEVICE

The experimental set-up consists of 11 cylindrical segments each 10 cm long and one 2·5 cm element, forming one long tube with an internal diameter of 5 cm (Figure 1).

The first segment has eight small tubes injecting air radially into the main tube. The flow rate varies during the experiments between 5 and 20 m^3/h (corresponding to an average flow speed of 4·4–17·6 m/s at the diaphragms or to a Reynolds number based on d of $6 \times 10^3 \leqslant \mathrm{Re} \leqslant 2{\cdot}3 \times 10^4$). A pair of diaphragms separated by

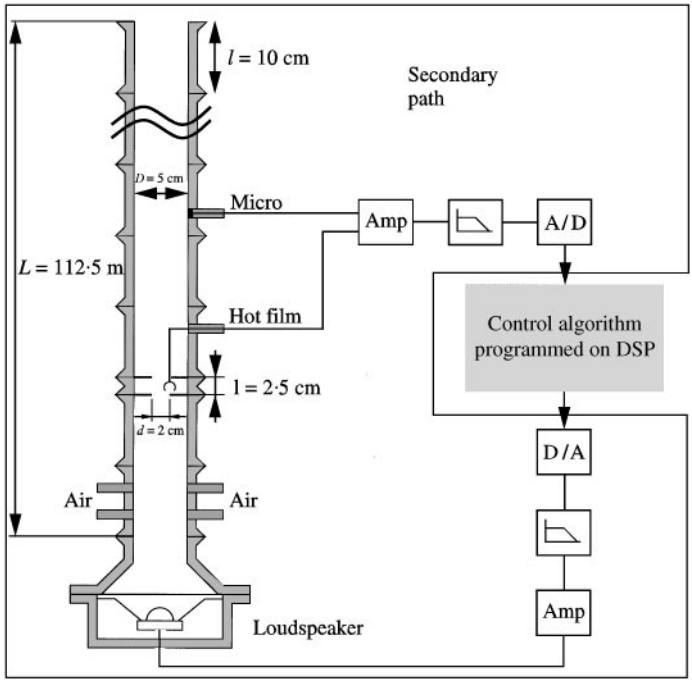

Figure 1. Experimental set-up. The pressure signal is measured by a microphone, the flow velocity by hot-film anemometer. The loudspeaker serves as actuator during control. The secondary path is given by the transfer function between the output of the DSP and its input (inside the thick line).

the small segment creates a cavity, where periodic vortex shedding takes place. The cavity is placed above the second segment. This geometry (ratio of cavity length and depth, length of the tube) was inspired by previous studies of Nomoto and Culick [3], Culick and Magiawala [4] and Dunlap and Brown [5]. As will be shown below, it guarantees relatively "clean" acoustics.

For control purposes, a flush-mounted microphone (Brüel & Kær 1/4″ type 4136) is placed 22·5 cm above the second diaphragm. The measured pressure oscillations are amplified, filtered and converted into a digital signal. In addition, a hot-film anemometer is placed in the cavity to detect the velocity fluctuations. The acoustic component of this signal is in general smaller than the fluctuations caused by turbulence or coherent vortical structures and therefore the main part of the signal detected is assumed to be due to aerodynamic phenomena. This signal is filtered, amplified and converted into a digital signal.

These signals serve as input to the control algorithms, programmed on a TMS320C31 processor (A/D converter, processor and D/A converter hosted on a DS1102 dSPACE board). The controller output then passes through a D/A converter, filter and amplifier and finally drives a 13 cm diameter loudspeaker fixed at the base of the tube.

The transfer function between the output of the control algorithm and its input will be denoted as "secondary path" (enclosed within the solid line in Figure 1). Later, this transfer function will play an important role in the different control algorithms.

3.2. AEROACOUSTIC PHENOMENA

It is first useful to determine the acoustic modes of the system. A band-limited white noise signal, generated on the processor, was used to excite the system. The system response is measured with the microphone. The complex transfer function between the system response and the white noise signal is calculated by

$$T_{xy} = P_{xy}/P_{xx}, \tag{1}$$

where P_{xy} is the cross-spectral density from the input of the secondary path to its output and P_{xx} is the power spectral density of the input of the secondary path.

The transfer function amplitude and phase are shown in Figure 2. Peaks in the spectrum correspond to higher gain and may be attributed to resonant acoustic modes. This introduces poles in the transfer function and additional phase lag (see the lower plot in Figure 2). On the other hand, nodes in the amplitude plot correspond to zeros in the transfer function. The phase lead generated in these cases can also be seen in the lower plot in Figure 2.

The peaks appearing in the spectra are compared in Table 1 with the calculated values. The method for calculating the longitudinal acoustic modes in the installation is described in reference [12]. Experimental and theoretical values are in good agreement. The acoustic boundary conditions were chosen as open without end correction for the lower extremity and open with end correction for the upper

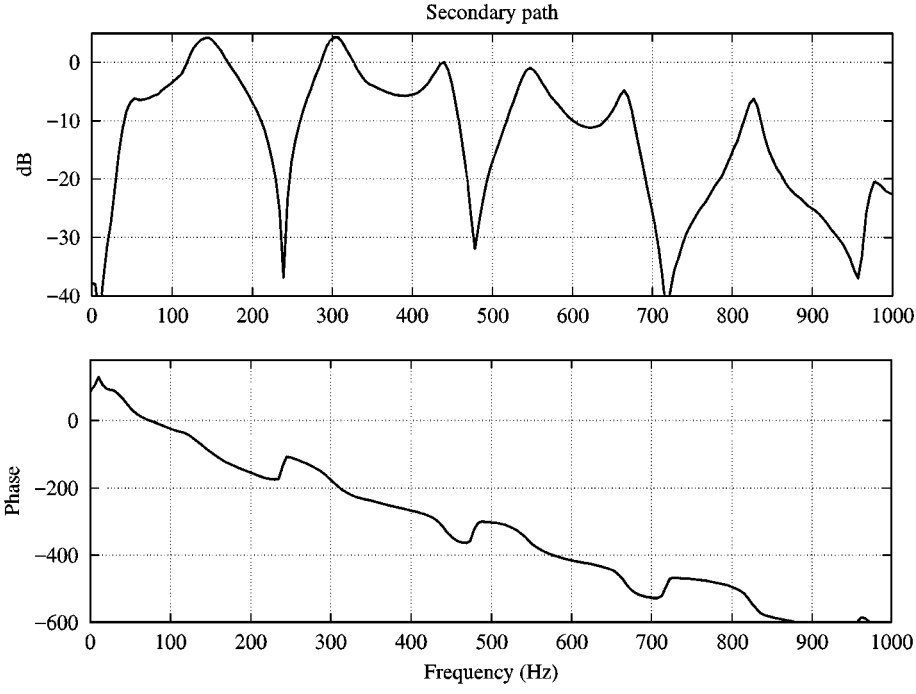

Figure 2. Identification of acoustic modes. Amplitude (upper plot) and phase (lower plot).

TABLE 1

Comparison of acoustic modes, experiment and theory. The error is calculated with respect to the experimental values

Experiment	Theory	Error (%)
140 Hz	139 Hz	—
300 Hz	280 Hz	7
440 Hz	417 Hz	5
545 Hz	548 Hz	—
665 Hz	677 Hz	2
820 Hz	791 Hz	3
975 Hz	902 Hz	7
1080 Hz	1035 Hz	4
—	1170 Hz	—
1340 Hz	1300 Hz	3

section. The error shown in the table is calculated with respect to the experimental values. The resonant frequencies determined experimentally are represented by horizontal lines in Figure 3.

Air is now injected into the system. The flow rate varies from 5 to 20 m^3/h, in steps of 0·5 m^3/h. Different frequencies appear in the spectrum, depending on the

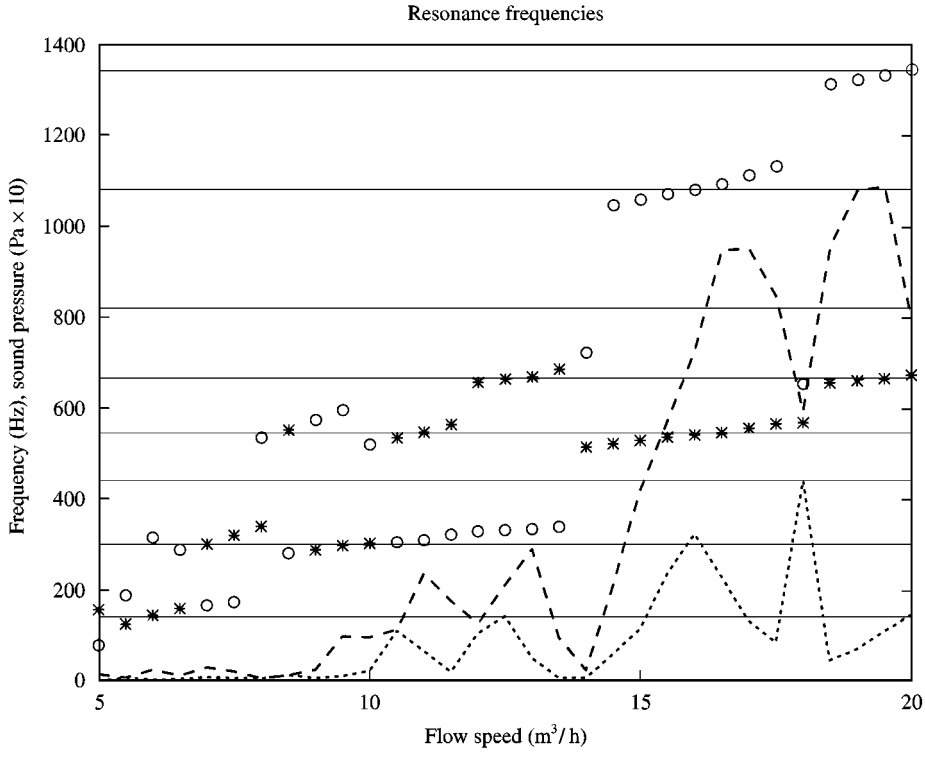

Figure 3. Coupling of convective modes with acoustics. (——) acoustic modes. Frequencies (∗) and corresponding amplitudes (- - - -) of the most energetic modes. Frequencies (○) and corresponding amplitudes (· · · · ·) for the second most energetic modes.

flow speed. The two strongest modes for each flow rate together with their amplitudes are represented in Figure 3. These frequencies are close to the acoustic modes identified previously. It is interesting to note that, as the flow speed increases, the excited frequency increases slightly until it "jumps" to another acoustic mode.

This phenomenon is typical of coupling between convective and acoustic modes and is reported in different publications dealing with instabilities in large segmented solid motors.

As shown in references [2, 5, 13] for example, the fundamental and the second harmonic are amplified by placing the restrictor pair at a pressure node (or velocity anti-node) for the fundamental longitudinal acoustic mode. The first harmonic could be amplified by placing the cavity at a pressure anti-node for the fundamental, which corresponds to a pressure node for the first harmonic (see reference [5]). In the present case, only the second and fifth harmonic are not present in Figure 3 (they appear only weakly in the spectra). Using "open" boundary conditions at the inlet and exhaust, the cavity is placed close to a pressure node for certain frequencies and close to an anti-node for others. This can be seen in Figure 4, which shows the mode shapes for different eigenmodes (experimental values) in the theoretical geometry with respect to the position of the cavity (shown

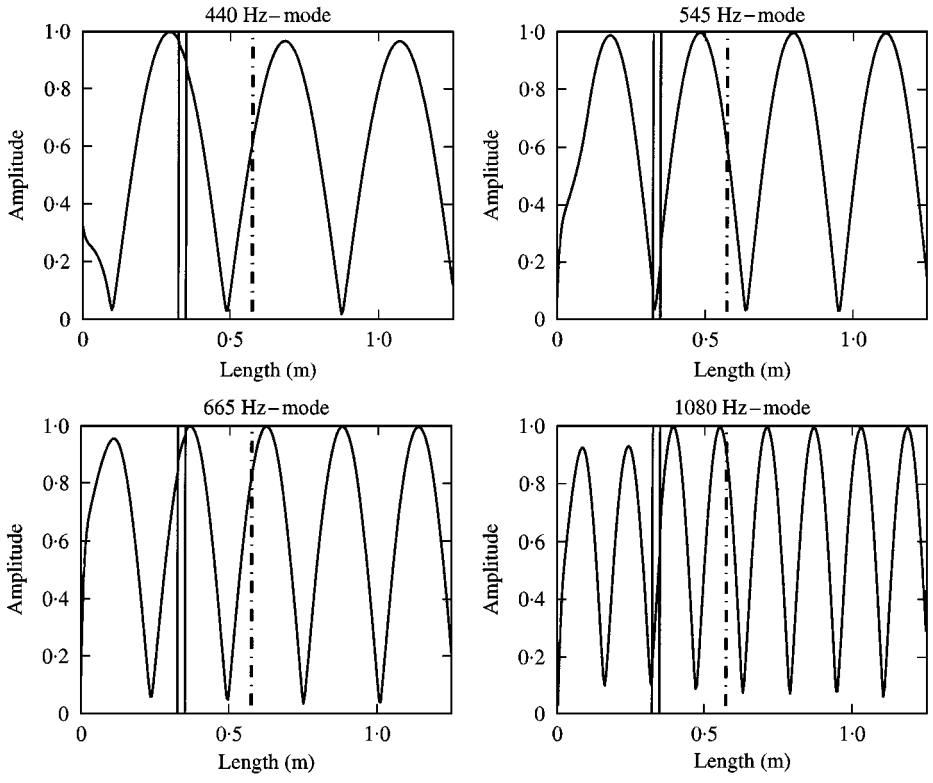

Figure 4. Mode shapes for different resonant frequencies with position of the cavity (——) and of the microphone (– – –).

by solid lines) and the microphone (shown by the dash-dotted line). Note the non-zero amplitude for the 440 Hz mode at the inlet of the set-up; this is due to the difference between the theoretical eigenmode (417 Hz) and the experimental value. The latter "does not fit" exactly in the given geometry.

Following the conclusions of Dotson *et al.* [2] and others, the magnitude of the excited frequency is now, amongst others, determined by the position of the cavity with respect to the eigenmode. Therefore, the 440 Hz mode, for which the cavity is close to a pressure anti-node, should not be excited very strongly. This can be verified in Figure 3. On the other hand, the 545 and 1080 Hz modes, where the cavity is close to a pressure node, are among the strongest peaks in Figure 3. Only the strong amplitude of the 665 Hz peak cannot be explained here, as Figure 4 indicates that the cavity is placed close to a pressure anti-node and not close to a pressure node.

It is natural that, by changing the position of the cavity inside the tube, other acoustic eigenmodes can be excited.

A simple model of the phenomenon described here is given in Figure 5, which shows the aeroacoustic loop leading to strong pressure oscillations. Vortical structures are shed behind the first diaphragm, travelling downstream and creating an acoustic signal when impinging on the second diaphragm. This acoustic signal travels upstream and helps, under certain conditions, to organize the vortex

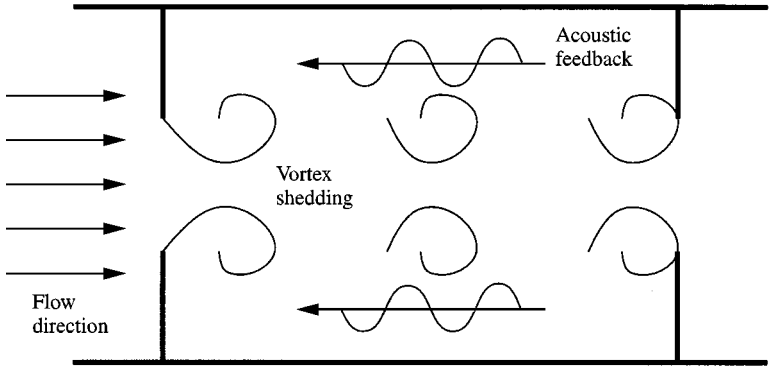

Figure 5. Feedback loop for the aeroacoustic phenomenon.

shedding. Therefore, the acoustics triggers the vortices, which, in turn, lead to new acoustic fluctuations. Hence, the feedback loop is closed. A similar reasoning for the acoustic coupling phenomenon in SRMs is given, for example by Vuillot [14].

This feedback model has been developed by Rossiter [15] and was used by Rockwell [16] for oscillations in boundary layers and by Dotson *et al.* [2] for the analysis of SRM data of the American space shuttle.

Related studies on aeroacoustic feedback are due to Chanaud and Powell [7]. Jet-edge and jet hole systems were investigated. Aerodynamic acoustic feedback was also observed in other configurations. Wright [18], for example, developed a theory for explaining the generation of boundary discrete tones emitted by aerofoils.

3.3. CONTROL ALGORITHM

Before describing control details, it is useful to represent the experimental set-up and the phenomena in terms of "black-box" transfer functions. This will be used in the design of the algorithms.

The overall system to control which is "seen by the control algorithm" is the secondary path (see Figure 1), which includes the D/A converter, filter, amplifier, the duct, the microphone, amplifiers, filter and finally the A/D converter.

For the specific application considered here, it is now useful to divide this secondary path **S** into sub-elements **S1**, **S2** and **S3**, as shown in Figure 6 (as the sensor is given by the microphone, **S** is an "acoustic path"; this changes, if, for example, a hot film is used). **S1** corresponds to the transfer function from the controller output to the first diaphragm in the tube, **S2** represents the transfer function to the microphone and **S3** the path from the microphone to the input of the control algorithm.

The aeroacoustic feedback loop described in the last section in Figure 5 is now included in Figure 6. Behind the first diaphragm the following scenario is hypothesized: velocity fluctuations introduced by the acoustic signal d^* together with velocity fluctuations induced by the air flow form correlated vortices u' which travel downstream and impinge on the second diaphragm. The acoustic signal

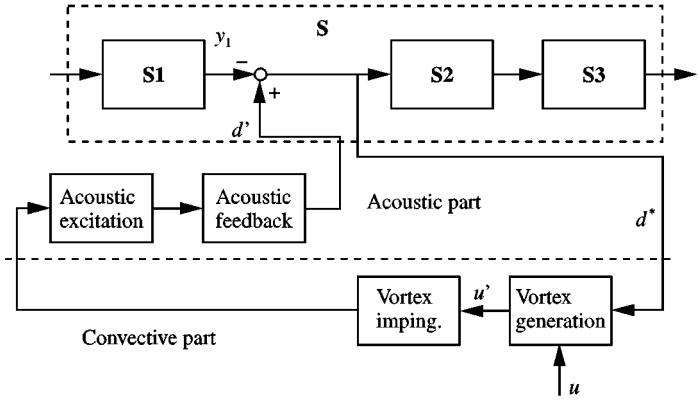

Figure 6. Detailed secondary path with model of the aeroacoustic phenomenon.

created in this process is fed back to the first diaphragm, where it arrives as d'. There it superposes, with y_1, the signal from the control algorithm, to give d^*. In fact, as d^* triggers the vortex shedding in the model, the controller can act at the source of the pressure oscillations, the vortex shedding and hence a "noise source controller" may be designed on this basis. Even if the influence of y_1 on d^* is neglected, the controller can be viewed as an "anti-noise algorithm", where the aim is just to counteract d'. These two "models" lead to two different design approaches, which will be discussed in the following section.

Before developing the control scheme, it is useful to replace the summing point where d' and y_1 superpose with a summing point outside the secondary path **S**. This is valid in the limit of linear transfer functions **S1**, **S2** and **S3** where the superposition principle holds. Now, the noise to be controlled (the primary noise) is denoted by d and the signal coming from the controller (having passed the secondary path) is denoted by y_r. The advantage of this transformation is obvious. The complete system **S** now appears separately and the noise to be controlled is superposed "outside" of **S**. One may then distinguish two control schemes: an anti-noise controller (Figure 7) and a noise source controller (Figure 8).

3.3.1. *The anti-noise controller*

For the anti-noise controller in Figure 7, the influence of the controller action on the primary noise d is neglected. As described before (see Figure 6), a signal y_1 equal to d' is to be created. In this optimal case, the sensor signal would be zero and therefore the noise would be perfectly controlled. In the notation of Figure 7, optimal operation ($e = 0$) means that the controller output, having passed **S**, has to become equal to d: $y_r = d$. It would now be useful to have an estimate signal $\hat{d}$ at the input of **W**, which is correlated to the primary noise d (in an "optimal" case, d would be used directly). Then **W** has to become the inverse of **S** for optimal control. With a perfect estimation, $\hat{d} = d$ and

$$e = d - y_r = d - \mathbf{SW}d = (\mathbf{I} - \mathbf{SW})d. \tag{2}$$

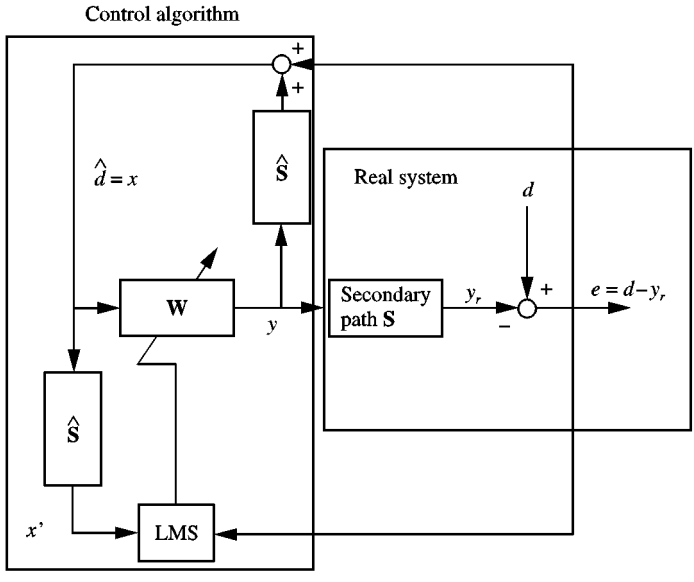

Figure 7. Anti-noise controller with filtered—x LMS update for the coefficients of **W**. $\hat{\mathbf{S}}$ is an estimate of the physical system described by a numerical filter.

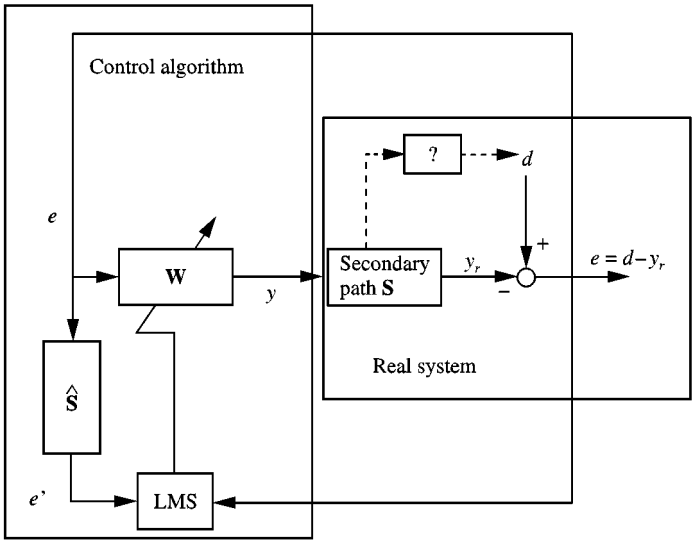

Figure 8. Noise-source controller with filtered—e LMS update of the coefficients of **W**. $\hat{\mathbf{S}}$ is an estimate of the physical system described by a numerical filter.

Hence, if a vanishing output $e = 0$ is to be achieved (and d cannot be changed), **W** has to become $\mathbf{S}^{-1}$. The estimation of the primary noise is given by

$$\hat{d} = e + \hat{\mathbf{S}}y = d - (\mathbf{S} - \hat{\mathbf{S}})\,y. \tag{3}$$

In the limit $\hat{\mathbf{S}} = \mathbf{S}$, $\hat{d}$ becomes identical to d.

The controller consists of an adaptive finite impulse response (FIR) filter. Its coefficients are updated using the well-known filtered-x LMS algorithm (see, for example, reference [19]): in order to compensate for the secondary path, the controller input has to be filtered by an estimation of the secondary path $\hat{\mathbf{S}}$ before the signal can be used to update the coefficients of $\mathbf{W}$. The estimation $\hat{\mathbf{S}}$ of the secondary path is obtained by identification before control. In fact, the task of the controller is to minimize a cost function $\hat{\xi} = e^2$, which depends on the controller action and therefore on the coefficients $\mathbf{w}$ of the adaptive filter $\mathbf{W}$. Hence, the coefficients $\mathbf{w}$ have to change to minimize the cost function. Starting with an arbitrary initial set $\mathbf{w}_0$, the filter coefficients change at each iteration in the direction of the gradient of $\hat{\xi}$ with respect to $\mathbf{w}$. With $x = \hat{d}$, this can be written as

$$\mathbf{w}_{k+1} = \mathbf{w}_k - \mu' \frac{\partial e_k^2}{\partial \mathbf{w}} = \mathbf{w}_k + \mu e_k \mathbf{S}\mathbf{x}_k. \tag{4}$$

As $\mathbf{S}$ is not known, the estimation $\hat{\mathbf{S}}$ is used. This finally leads to

$$\mathbf{w}_{k+1} = \mathbf{w}_k + \mu e_k \underbrace{\hat{\mathbf{S}}\mathbf{x}_k}_{\mathbf{x}'_k} \tag{5}$$

with $\mathbf{w}_k$ denoting the coefficient vector of $\mathbf{W}$ and μ the step size, e_k is the error signal measured by the microphone and $\mathbf{x}_k$ denotes the vector containing the estimated values of the primary noise. The index k indicates the kth time step. There are many applications of anti-noise control described in the acoustics literature; see, for example, the books by Nelson and Elliot [20] or Kuo and Morgan [21].

3.3.2. *The noise source controller*

The noise source controller now assumes the imposition of an action of the controller on the primary noise itself. Although a physical model of this action is not necessary for the control algorithm (as indicated in Figure 8 by a ?-symbol), it will be useful to give a qualitative description of how it works. As already described in Section 3.3. (see also Figure 6), the vortex shedding is at the "origin" of the pressure fluctuations but it is also sensitive to the acoustic signal which triggers the periodic shedding. Thus, the phenomenon is a closed-loop, self-sustained type, and under appropriate conditions it will grow until non-linear effects bring it to a limit cycle.

The controller signal y_1 breaks into this loop and might reduce d^* (see Figure 6). Vortex shedding will decrease and the self-sustained loop will run in the opposite direction until d^* is small enough to prevent the periodic shedding of vortices and an essentially broadband acoustic noise is attained.

A small controller output will then be sufficient to maintain control (i.e., to keep the acoustic signal below the limit) where the self-sustained loop starts operating.

The necessary algorithm only differs slightly from the anti-noise scheme; here, the error signal e is directly used as input for the filter $\mathbf{W}$; this appears appropriate since the microphone signal is assumed to be proportional to the noise source. As may be

deduced from Figure 8, if e is small, a small control action y_r is sufficient to maintain control. In the limit of perfect control with $e = 0$,

$$e = d - y_r = d - \mathbf{SW}e, \quad (I + \mathbf{SW})e = d, \quad e = \frac{d}{(I + \mathbf{SW})}. \tag{6}$$

A vanishing error signal is only achieved (with bounded $\mathbf{w}$) for $d = 0$. Of course, this zero limit cannot be reached, as for $e = 0$, the primary noise cannot be controlled (the output of $\mathbf{W}$ would be zero and with zero control action, the instability cannot be controlled). Nevertheless, the controller will reduce the noise and the noise source until the sensor signal becomes broadband. Note the difference to the anti-noise algorithm: for the noise source controller $e = 0$ (or e small enough) means that $d = 0$ (or d small enough), whereas for the anti-noise controller $e = 0$ (or small e) means $y_r = d$ (or $y_n \approx d$). In the anti-noise control scheme no action on d is necessary to achieve control. For the optimal control case ($e = 0$), the difference between the two schemes may be understood by comparing equations (2) and (6) or by examining the block diagrams given in Figures 7 and 8.

As for the anti-noise controller, the cost function $\hat{\xi} = e^2$ is to be minimized. Hence, the coefficients of $\mathbf{W}$ have to change so as to minimize $\hat{\xi}$. As the influence of the controller on d cannot be specified explicitly, the final values of $\mathbf{W}$ cannot be determined as in the anti-noise case. Nevertheless, taking an arbitrary initial set $\mathbf{w}_0$ and changing its values in the direction of the gradient of $\hat{\xi}$ with respect to $\mathbf{w}$ leads to

$$\mathbf{w}_{k+1} = \mathbf{w}_k + \mu' \frac{\partial e_k^2}{\partial \mathbf{w}} = \mathbf{w}_k + \mu e_k \hat{\mathbf{S}}\mathbf{e}_k. \tag{7}$$

The idea of using an acoustic signal for acting at the source of flow instabilities is used in earlier studies, for example by Ziada [9]. In contrast to that work, in these experiments the loudspeaker is not placed close to the noise source, nor directed towards it. Nevertheless, using a feedback controller, it will be shown that the noise level may be reduced significantly by acting on the noise source.

It is also possible to use other sensors to generate an input signal to the control algorithm. If the sensor signal is correlated with the phenomenon to be controlled, the algorithm can diminish the instability by acting in an appropriate way. It is important to note that the secondary path information needed by the controller should be available for these cases. Also, for controllers with a fixed secondary path (as in the examples discussed here), it is important to chose a sensor so that this path does not change too much during operation of the device. If this is not the case, the control algorithm will diverge. Therefore, a convective secondary path (corresponding to a hot-wire probe, for example) can only be used in a limited range of flow velocities.

A combination of different sensors can also be used as input for control. Taking the microphone as error sensor (the acoustic secondary path does not change much during operation) in combination with the hot wire at the input of the controller yields good results (although the way the controller acts changes from a feedback

type to a feedforward one; the same scheme can be used as in Figure 8). As the hot film is also sensitive to the flow turbulence, the input of the controller, even in the controlled case, is much noisier than the microphone signal. This leads to problems for the algorithm which finally result in a reduced performance compared with the arrangement with one microphone presented in Figure 8.

3.4. INFLUENCE OF THE LEAK ON THE CONTROLLER FILTER COEFFICIENTS

There are several advantages in using adaptive FIR filters. The error surface of $\hat{\xi}$ is a quadratic function of the filter coefficients and therefore there is only one minimum for a certain combination of coefficients which is the global one. In addition to that, FIR filters only have zeros and are therefore always stable. There are no problems with unstable poles and local minima as for adaptive IIR filters. Consequently, there should be no problems during the adaption. Nevertheless, the proper convergence of the LMS algorithm depends on the properties of the input to the adaptive filter. Insufficient spectral excitation of the filter due to the input signal may result in divergence of the filter coefficients. In this case, the solution for the minimization procedure of the algorithm is not unique and finite precision effects in real-time implementations lead to unconstrained growth of the weights (see reference [21]). The introduction of a leakage factor into the update law can prevent this effect. It can be shown that this corresponds to the addition of low-level white noise for the input signal, which leads to sufficient spectral excitation of the algorithm. The modified update algorithm for the controller shown in Figure 8 is given by

$$\mathbf{w}_{k+1} = \nu \mathbf{w}_k + \mu e'_k e_k \tag{8}$$

with $0 < \nu \leqslant 1$. If the leakage factor $\nu = 1$, the original update law without leak is obtained.

As shown earlier, the cost function to be minimized by the LMS algorithm without leak is given by

$$\hat{\xi} = e_k^2, \tag{9}$$

which corresponds to a minimization of the squared instantaneous error signal. It can be shown that the leak also has an influence on this function, which can be rewritten for the modified leaky algorithm as:

$$\hat{\xi} = e_k^2 + \gamma \mathbf{w}_k^{\mathrm{T}} \mathbf{w}_k \quad \text{with } \gamma = \frac{1-\nu}{\mu}. \tag{10}$$

Again, setting $\nu = 1$ gives the original cost function without leak. This new cost function $\hat{\xi}$ can be interpreted as follows: the uncontrolled growth of the filter weights (which corresponds to an uncontrolled growth of the controller output) is penalized. Hence, the introduction of a leak also prevents the output signal from being overdriven. This can be useful if overdriving leads to non-linear behaviour of the secondary path which is not taken into account by the linear model $\hat{\mathbf{S}}$.

A comparison of results with and without leak is given in the next section together with other experimental results.

4. EXPERIMENTAL RESULTS

4.1. IDENTIFICATION OF THE SECONDARY PATH

The identification of the secondary path is carried out in the configuration shown in Figure 9: a white noise signal x_k, generated on the DSP, excites the secondary path **S**. The response y_k is measured and compared with the response of $\hat{\mathbf{S}}$, $\hat{y}_k$. $\hat{\mathbf{S}}$ is an adaptive 110 element FIR filter. The task during the adaption process is to minimize $\hat{\xi} = e_k^2$. The sampling frequency in the examples shown here is 5 kHz. Figure 10 shows the effect of the adaption in the time domain. The difference $e_k = y_k - \hat{y}_k$ becomes significantly smaller and the squared error, averaged over 50 values is close to zero after adaption. In the frequency domain, the amplitude and the phase of the real secondary path and its estimation are compared in Figure 11. It can be seen that there is also a very good agreement in the frequency domain for the frequency range of interest. These results show that $\hat{\mathbf{S}}$ is a good estimation of the input–output behaviour of the real secondary path **S**. This estimation can now be used for the different control algorithms introduced earlier. For the implementation in the DSP, the values of $\hat{\mathbf{S}}$ are now fixed and the program can be switched from the identification to the control mode.

It is important to know whether the presence of the air flow changes the secondary path. In this case, the model of $\hat{\mathbf{S}}$ used in the different algorithms would probably not be sufficiently precise in order to guarantee the convergence of the adaptive algorithms. For all algorithms presented here, the update of the controller coefficients depends on the filtered e or the filtered-x signal, the controller input filtered by $\hat{\mathbf{S}}$. If this filtering leads to a phase error (with respect to the real **S**) of more than $\pm 90°$, the adaption of **W** will fail.

In order to verify that the secondary path does not change too much with the air flow, the identification of **S** has been made with different volume flow rates (0, 6, 12

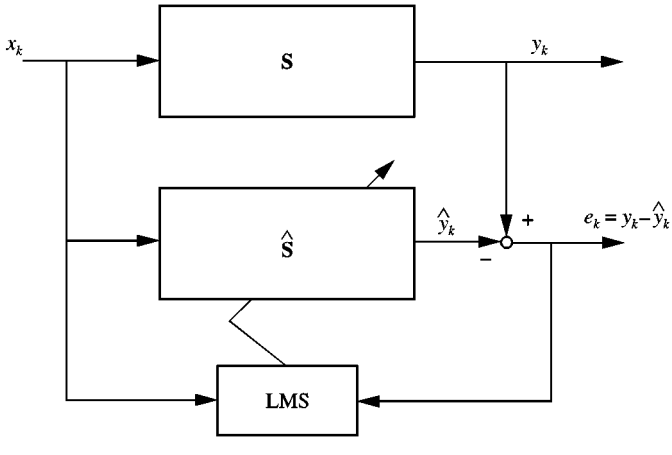

Figure 9. Adaptive identification of the secondary path $\hat{\mathbf{S}}$.

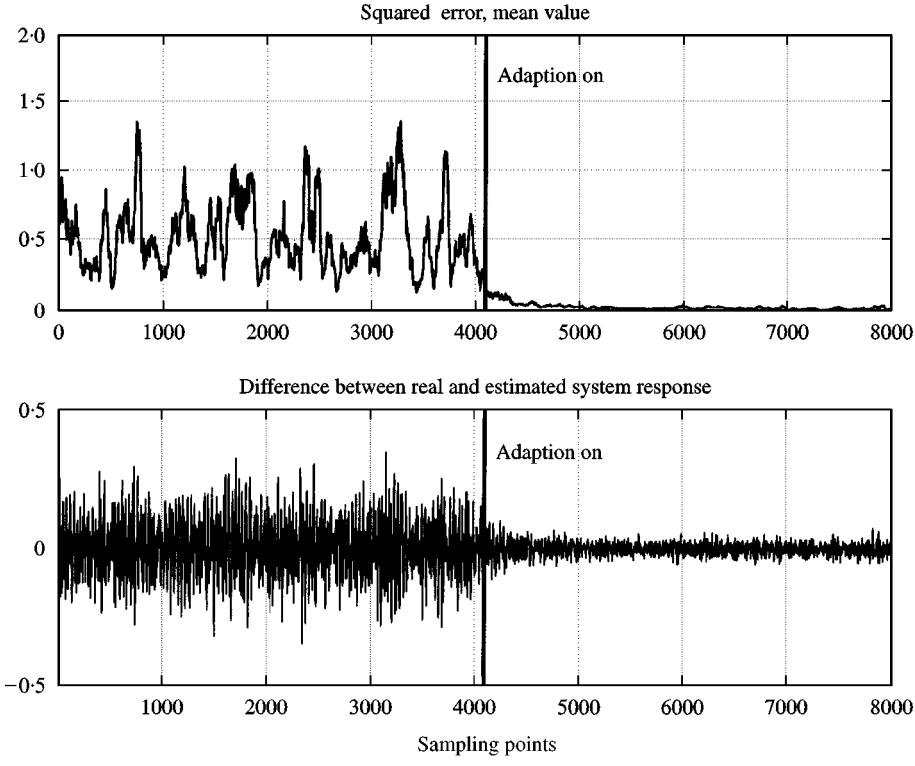

Figure 10. Adaption of the secondary path, time domain. Upper plot: squared error, mean value. Lower plot: error.

and 18 m^3/h). In this case a chirp signal (80–1500 Hz, $\tau = 1$ s) has been used in order to excite the system. The chirp leads to a better input/output correlation and, as the same tests have been made with the hot film, allow, in this case, well-correlated signals to be obtained. As can be seen in Figure 12, the transfer function amplitudes do not change significantly in the presence of the air flow. For $\dot{V} = 18\ m^3$/h for example, the mode at 545 Hz is shifted towards 600 Hz. This arises from the frequency peak created by the aeroacoustics, which is for $\dot{V} = 18\ m^3$/h slightly higher than the acoustic mode (compare with Figure 3). Also, the phase does not change significantly. As the system response becomes relevant for frequencies above about 100 Hz, the phase only becomes well defined for these frequencies. Therefore, the difference in the phases of $\pm 180^\circ$ which appear in Figure 12 for frequencies below 100 Hz is of no importance. Therefore, the air flow does not change the acoustic path and hence the secondary path identified without flow can be used for the controller algorithms.

A hot wire as sensor for the control can now also be considered. The secondary path then becomes "semi-convective" as it represents in this case the transfer function from an acoustic actuator signal to a velocity sensor. It is easy to understand that the varying air flow now influences the secondary path. Hence, it will not be constant for different air flows and consequently an approach with a fixed $\hat{\mathbf{S}}$ will only work for a limited range of $\dot{V}$. Algorithms with on-line

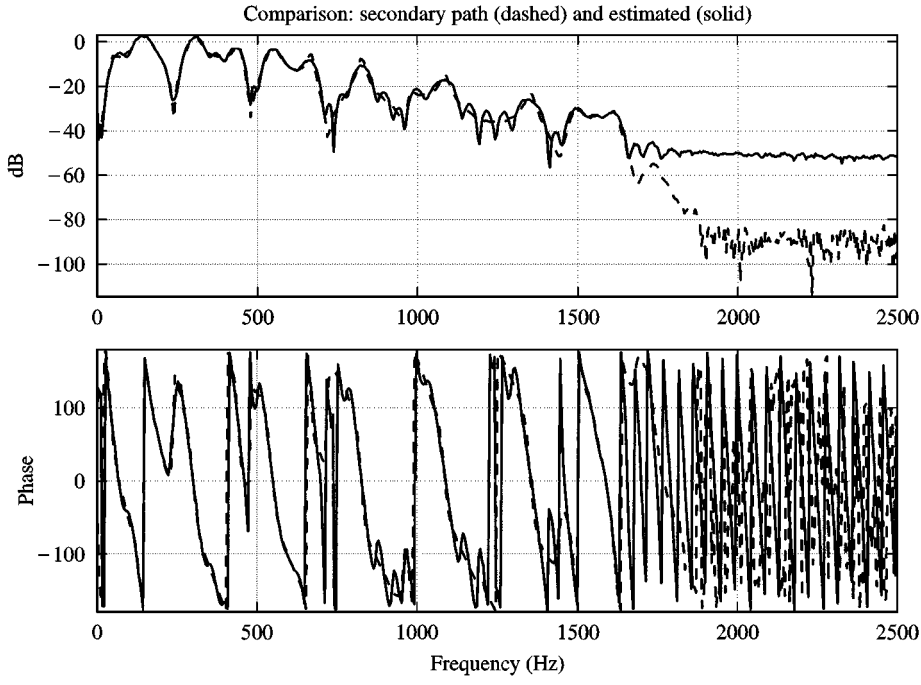

Figure 11. Adaption of the secondary path, frequency domain. Upper plot: amplitudes. Lower plot: phases. Estimated (——) and real values (- - - -).

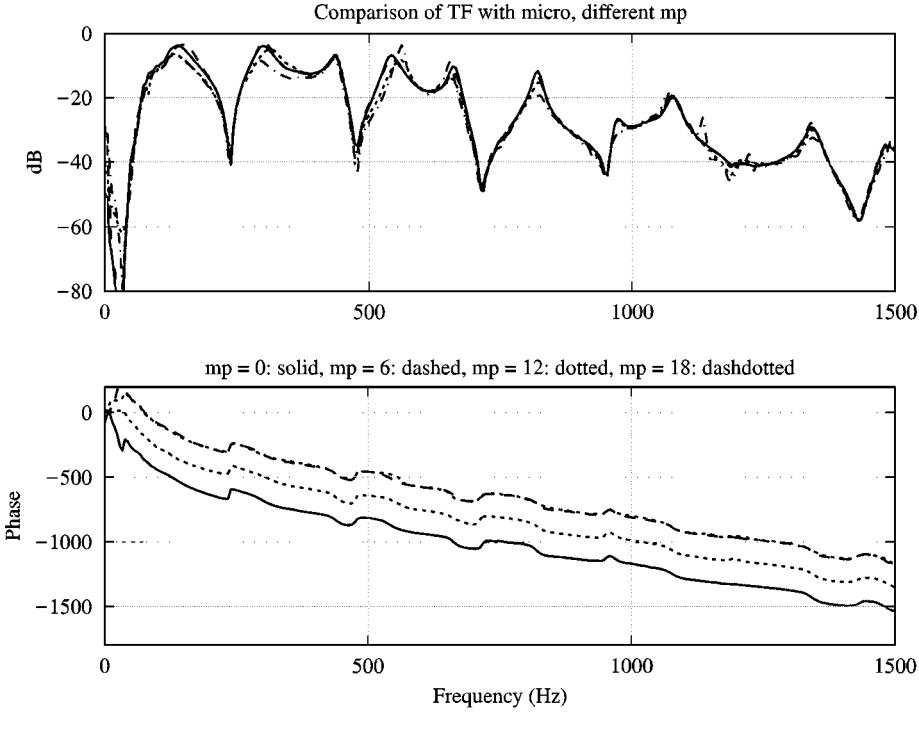

Figure 12. Transfer function of S for the microphone for different volume flow rates of air: $\dot{V} = 0$ (——), 6 (- - - -), 12 (· · · · · ·) and 18 (– – –) m^3/h. Upper plot: amplitudes, lower plot: phases.

identification of the secondary path would be necessary to obtain wider applicability.

4.2. INFLUENCE OF THE LEAK ON THE FILTER COEFFICIENTS OF W

As stated in section 3.4, the influence of the leakage factor on the adaption of the filter coefficients can be crucial for the algorithm.

The identification of the secondary path $\hat{\mathbf{S}}$ uses the original LMS algorithm. There, the coefficients are fixed after a short time of convergence and consequently the long-term problems of divergence of the filter coefficients do not play an important role. In addition, it should be pointed out that the white noise signal used during the identification persistently excites any order and hence only one set of filter parameters leads to a minimization of the error function. Therefore, even for a long-time adaption there should be no problems with divergence of the coefficients.

This changes during the control. The input of the loudspeaker depends on the behaviour of the system and it can theoretically reach large values which would overdrive the actuator. The controller also works over a long time period. As it should adapt to changes in the system, the filter coefficients are not fixed but updated during the whole process. The input of the controller is normally a signal containing only a few frequency components. In the real environment the signals are more or less noisy. However, as indicated in section 3.4 the controller coefficients may diverge under these conditions.

In order to investigate the different convergence properties, tests have been made with and without leak. The noise source controller using one microphone has been used. After identification of the secondary path, an air flow of 16 m^3/h was injected and the controller was switched on. The first 50 coefficients of $\mathbf{W}$ for different time instants (times are given with respect to the switching on of the controller) for the controller without leak can be seen in Figure 13. The first coefficients increase and would lead to a divergence of the algorithm (although the coefficients diverge, the controller still worked correctly when the experiment was stopped after 20 min. A divergence of the algorithms could be observed in other tests).

A leak was introduced during the second experiment. The filter coefficients in this case (Figure 14) stay nearly constant during the whole experiment.

The influence of the leak on divergence problems (as well as on the bounding of the output power) could be verified in this case. The additional computation time required by the leaky algorithm is clearly justified by the advantages introduced. A decrease of the controller performance could not be observed.

4.3. COMPARISON OF THE ALGORITHMS IN AN ANTI-NOISE SITUATION

In order to show the differences between the anti-noise and the noise source algorithms it is useful to test them in a purely anti-noise situation where the primary noise d cannot be changed by the controller action. Therefore, the experimental device is slightly modified.

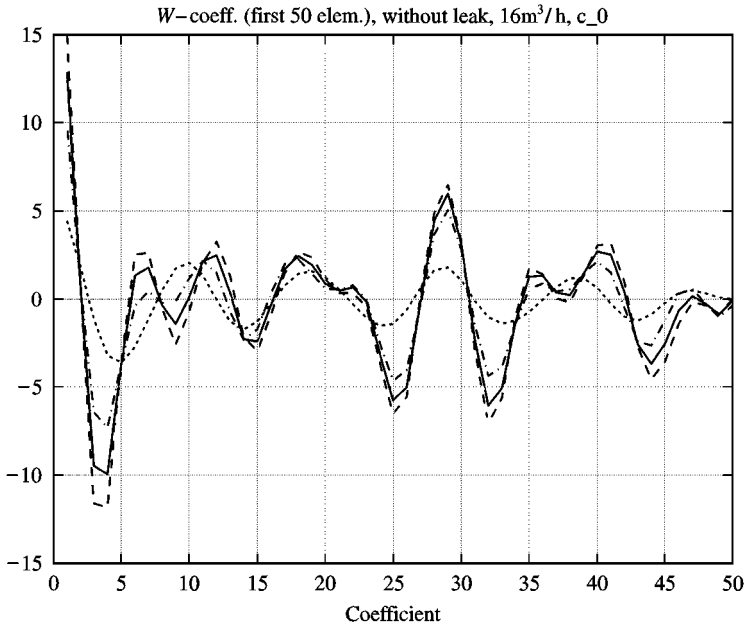

Figure 13. Filter coefficients of **W** for different time instants, without leak: · · · ·, $t = 1$ min; – · –, $t = 7$ min; ——, $t = 13$ min; – –, $t = 19$ min.

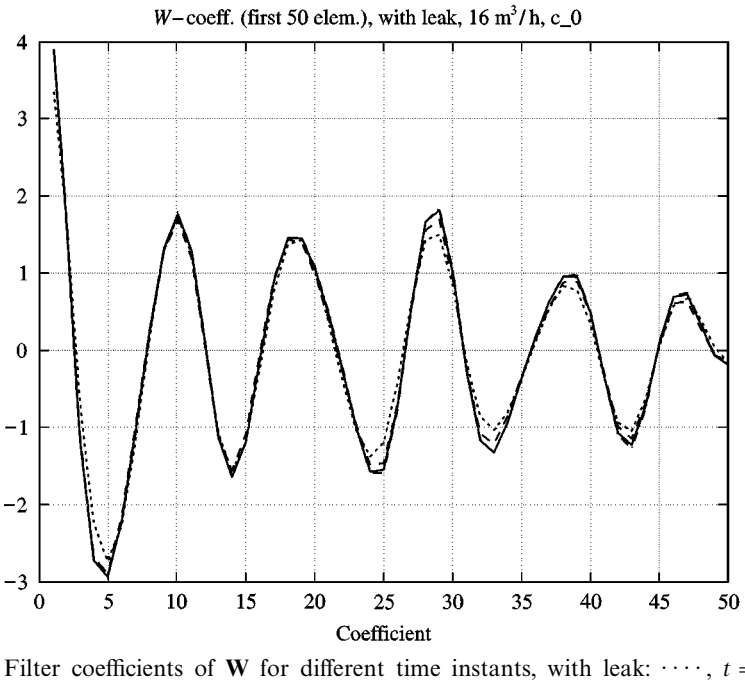

Figure 14. Filter coefficients of **W** for different time instants, with leak: · · · ·, $t = 1$ min; – · –, $t = 7$ min; ——, $t = 13$ min; – –, $t = 19$ min.

The primary noise which one wishes to control is delivered by a function generator and added to the system just before the low-pass filter used for the sensor signals. The frequency is close to the one excited by the air flow in the experiments

reported later in Figures 18, 19 and 22 (550 Hz). Note that the secondary path does not change with respect to the initial experiment. Following the identification procedure described in section 4.1, the set-up is run with the synthetic sinusoidal noise, without an air flow. For successful control, the algorithm has to counteract the primary noise: a signal with the appropriate frequency, amplitude and phase has to be generated and injected by the controller into the system.

The anti-noise controller reacts as expected (see Figure 15). After switching on of the controller (vertical line), the error signal (upper plot) diminishes as the controller output (lower plot) reaches the appropriate amplitude to counteract the primary noise. Steady state is characterized by a constant small error signal and a constant large amplitude in the controller output.

The noise source controller does not work in this configuration (see Figure 16). After a first phase where the error signal decreases continuously, it starts oscillating (upper plot) and this is also the case for the controller output (lower plot). There is no stable state. As the error signal diminishes, the controller output diminishes as well. But as the primary noise does not change, this leads to an increase of the error signal which leads to an increased controller output. Again, the error signal becomes smaller, the controller output changes. The amplitude maxima and minima of the error signal and the controller output are slightly shifted with respect to each other. This is due to the delay introduced by the physical system (mainly the filters and the acoustics)

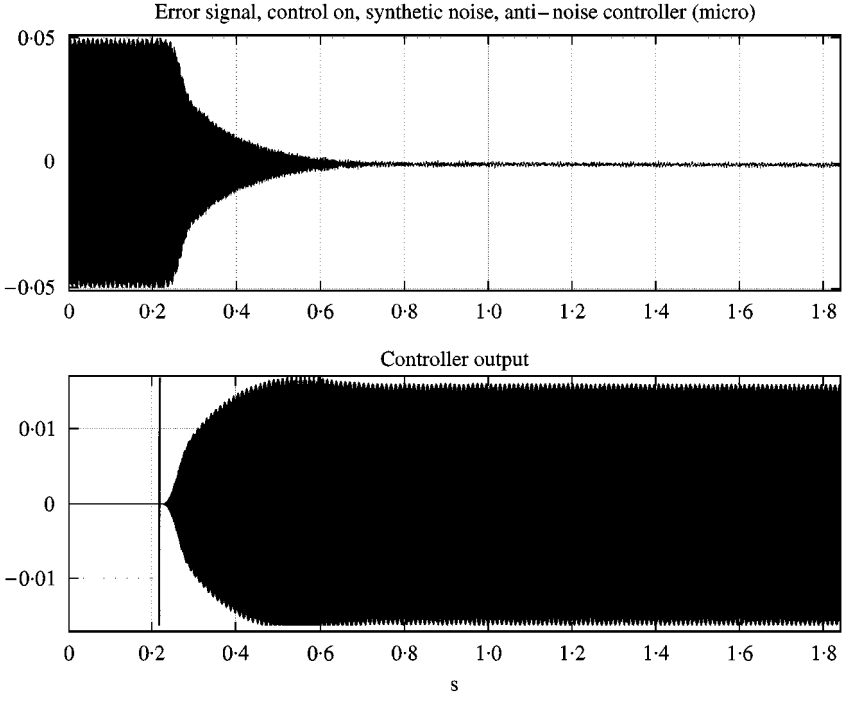

Figure 15. Error signal (upper plot) and controller action (lower plot) Anti-noise controller with synthetic noise. Controller switch on.

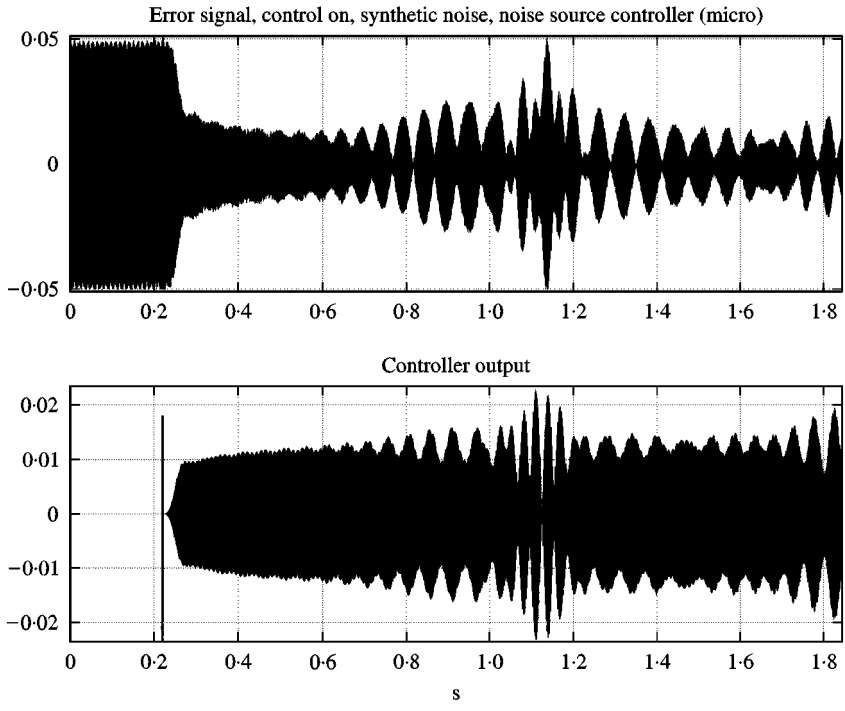

Figure 16. Error signal (upper plot) and controller action (lower plot). Noise source controller with synthetic noise. Controller switch on.

While the noise source controller does not work in this example, it will be shown in section 4.5 that significantly reduces the noise level in the case of an aeroacoustic instability. This will clearly indicate that the source of sound is sensitive to the sound itself.

4.4. ADAPTIVE CONTROL WITH ANTI-NOISE CONTROLLER

Control of the aeroacoustic instabilities was first carried out with the anti-noise controller. For fixed coefficients of $\hat{\mathbf{S}}$, the microphone signal spectrum was calculated for different air flows without and with control. The acquisition with the controller on was started after the convergence of $\mathbf{W}$ (a 200 element-FIR adaptive filter).

In addition, the estimation of the acoustic signal sent by the controller to the system (called *srd*) was used in order to estimate the acoustic power needed to control the phenomena. This estimation was calculated by taking the controller output and passing it through the estimated secondary path, $\hat{\mathbf{S}}$. It is assumed that this estimate approximates to the acoustics introduced by the controller.

Figure 17 shows the spectra for $\dot{V} = 16\ \mathrm{m}^3/\mathrm{h}$. Two peaks appear, the second being one octave higher than the first. The controller reduces these levels by 20–30 dB. On the other hand, during control a new peak appears at about 800 Hz, increasing the noise level at this frequency. The signal *srd* suggests that the 1100 Hz peak is controlled without significant controller action at this frequency: the action

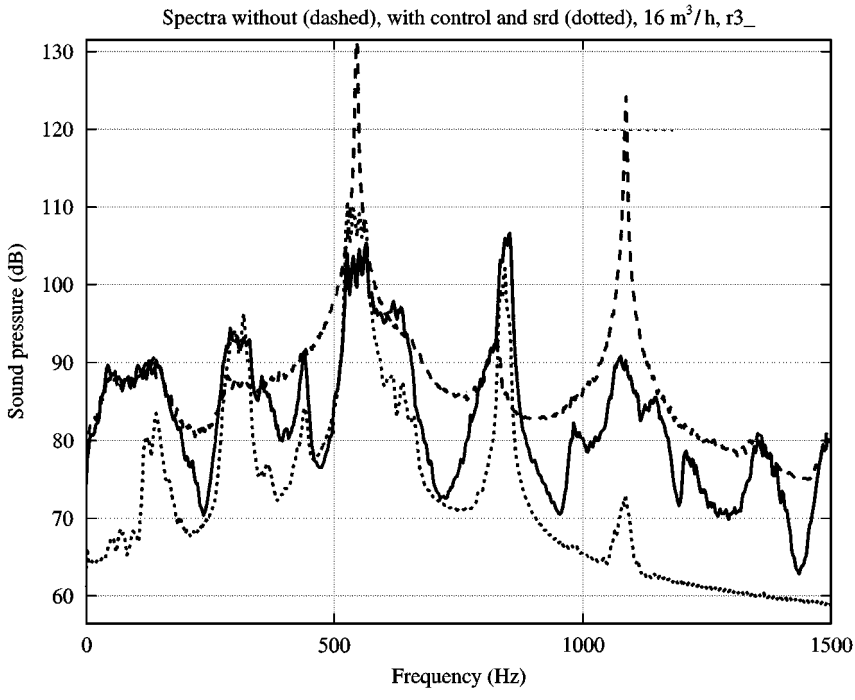

Figure 17. Spectra without (- - - -)/with (——) control and estimation of acoustics introduced by the controller (· · · · ·). Air flow rate $\dot{V} = 16\ \mathrm{m}^3/\mathrm{h}$.

on the fundamental 550 Hz appears to control the first harmonic also. Although, the 800 Hz component of *srd* appears to be at the origin of the increase of the noise level during control, tests indicate that this frequency component would reach larger values during control if the controller was not acting at this frequency. Nevertheless, the spectrum with control is much smoother than without and the controller achieves a significant noise reduction.

The influence of the controller on the error signal, the signal which is detected by the microphone, is shown in Figures 18 and 19. Having switched on the controller (see Figure 18), the controller calculates a strongly oscillating output at the beginning. This indicates that the controller, conceived as anti-noise controller, also modifies the source of the noise. In a pure anti-noise configuration, the controller output would grow up to the level necessary to counteract the primary noise. This level would then stay constant during control. After a certain time the controller reaches a kind of steady state (second half of the upper plot in Figure 19), which sometimes can be interrupted by new oscillations in the output, although this time being much smaller than at the beginning of the control. When the controller is switched off, the error signal grows approximately exponentially to reach the normal level without control.

Finally, the acoustic power in the system with and without control can be calculated and compared, and the acoustic power needed to accomplish the control may be estimated using *srd*. The acoustic power can be calculated by integrating the acoustic energy flux $\mathbf{I} = pv$ (with p the pressure and v the corresponding velocity)

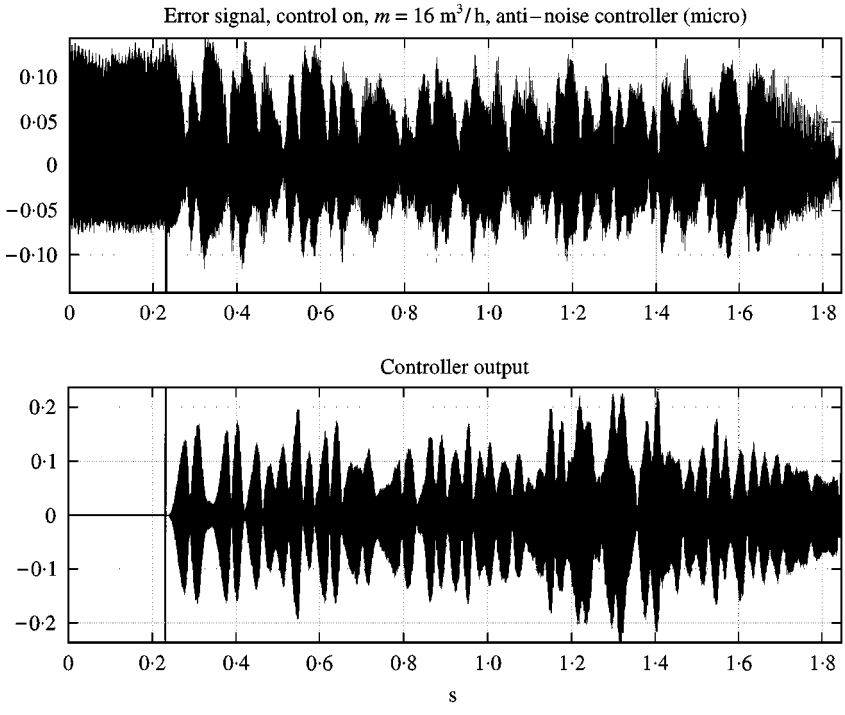

Figure 18. Error signal (upper plot) and controller action (lower plot). Air flow rate $\dot{V} = 16\ \mathrm{m}^3/\mathrm{h}$. Controller switch on.

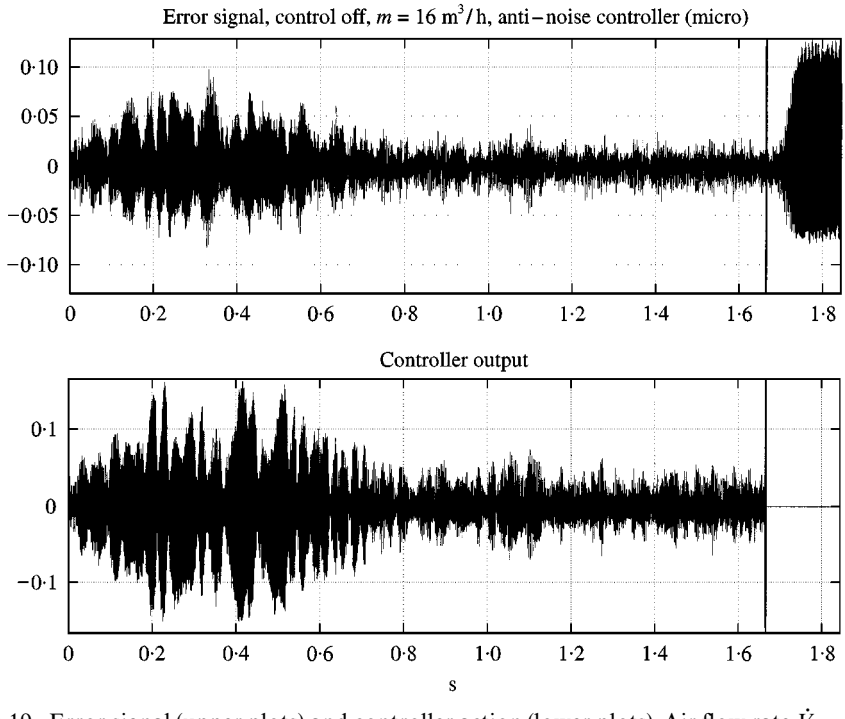

Figure 19. Error signal (upper plots) and controller action (lower plots). Air flow rate $\dot{V} = 16\ \mathrm{m}^3/\mathrm{h}$. Controller switch off.

over the surface through which it has passed. This can be written as

$$W_p = \int\int_0^{f_c/2} \frac{S_{pp}(f)}{\rho c}\,\mathrm{d}f\,\mathrm{d}A, \tag{11}$$

with $\mathrm{d}A$ the integration over the surface, $\mathrm{d}f$ the integration over the frequency band and $S_{pp}(f)$ the power spectrum estimate in $\mathrm{Pa}^2/\mathrm{Hz}$. The values of ρ and c are the density and sound speed of air.

Although the efficiency of the control varies with the air flow, the noise with control is always smaller than without. The gain is between 20% up to nearly 95% (see Figure 20). The acoustic power needed to accomplish this normally stays around or below 20% of the acoustic power which is in the system without control. For some flow speeds ($\dot{V}$ above 18 m^3/h and for $\dot{V} = 12{\cdot}5\ \mathrm{m}^3/\mathrm{h}$) the controller is less effective and requires a larger amount of acoustic energy. The difference in the effectiveness (between 20% and 95%) seems to be due to the peak-to-broadband noise ratio of the uncontrolled noise. In general, the higher and narrower the peaks, the better the controller acts upon it. If the peaks are not predominant over the broadband noise, the controller cannot determine a proper output and hence it cannot reduce the peaks. This is a general problem of a feedback noise controller, which can only act on periodic noise. The feedback controller has to predict the future primary noise values. This is only possible if there is a coherence between the

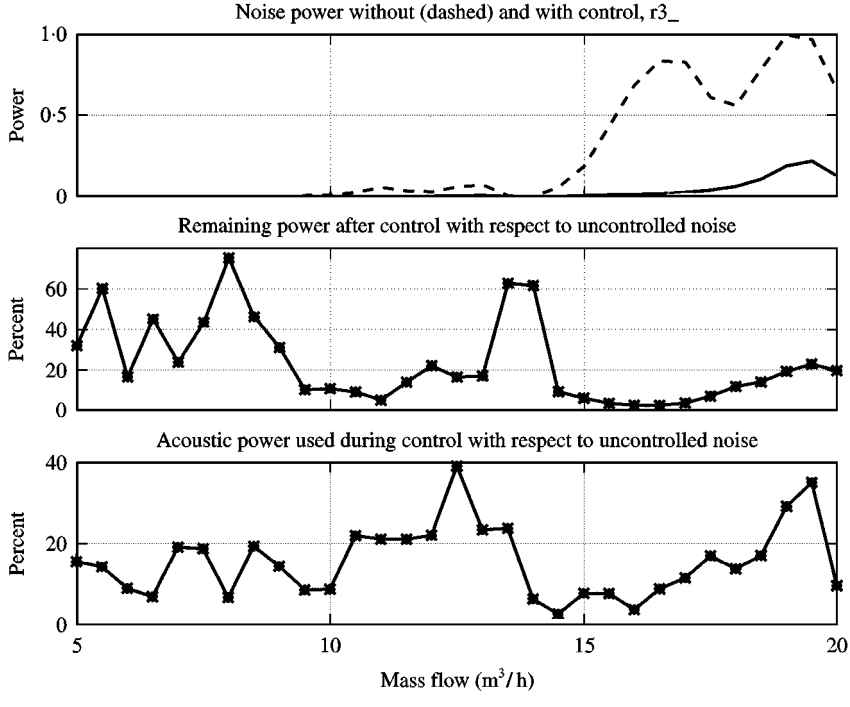

Figure 20. Comparison of the noise power with (——)/without (- - - -) control, normalized values (at the top), in percent (in the middle) and comparison *srd*/without control, in percent (at the bottom).

current and a future value; that is, the signal to be controlled must be periodic. The high values of energy required for $\dot{V} = 19$ and 19·5 m^3/h are mainly due to the fact that high-frequency peaks appear during control; the controller can only partially reduce these. These peaks even become the dominant ones during control. In addition, the controller is not able to maintain a constant low noise level. There are oscillations in the amplitude which have been described earlier.

4.5. ADAPTIVE CONTROL WITH NOISE SOURCE CONTROLLER

The same experiments have been carried out for the noise source controller. The spectra with and without control have been calculated for different air flows. Again, the controller filter length was 200 and the sampling frequency 5 kHz. Figure 21 displays the spectra without control (dashed line), with control (solid line) and the estimated *srd* (dotted line) for $\dot{V} = 16$ m^3/h. Again, the two main peaks are reduced significantly to the level of the broadband noise. Under control, the peak at 800 Hz is slightly increased. Compared to the anti-noise controller, the spectrum with control is even smoother and the noise reduction is more important.

An even more significant difference to the algorithm discussed earlier can be seen for the error signal (see Figure 22). The reduction in the error signal is obtained almost immediately after switching the controller. The controller output is displayed in the lower plot in Figure 22. Initially, this amplitude grows rapidly above the level which is later necessary to maintain control. This behaviour is

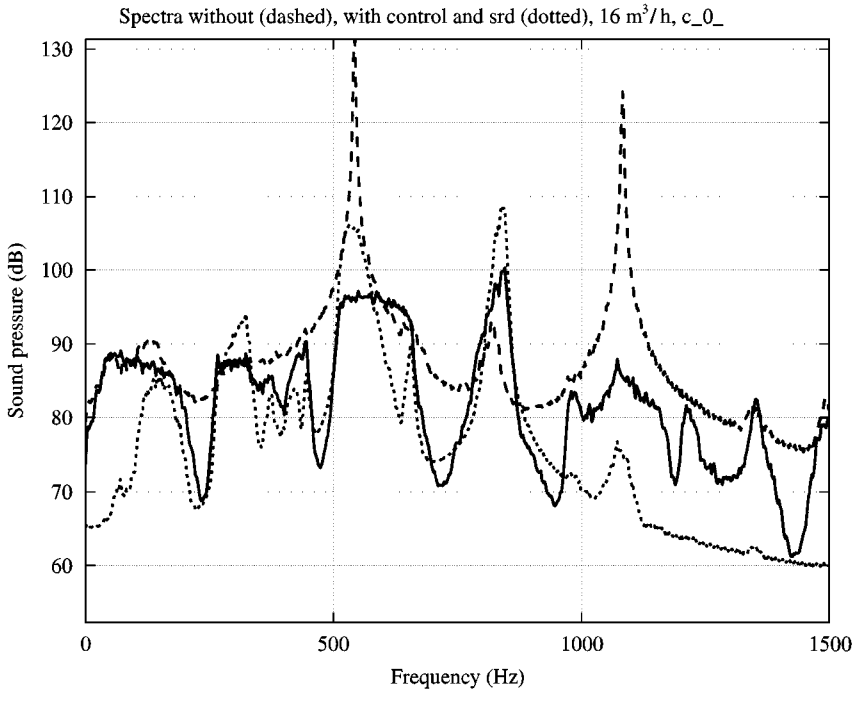

Figure 21. Spectra without (- - - -)/with (——) control and estimation of acoustics introduced by the controller (· · · · ·). Air flow rate $\dot{V} = 16$ m^3/h.

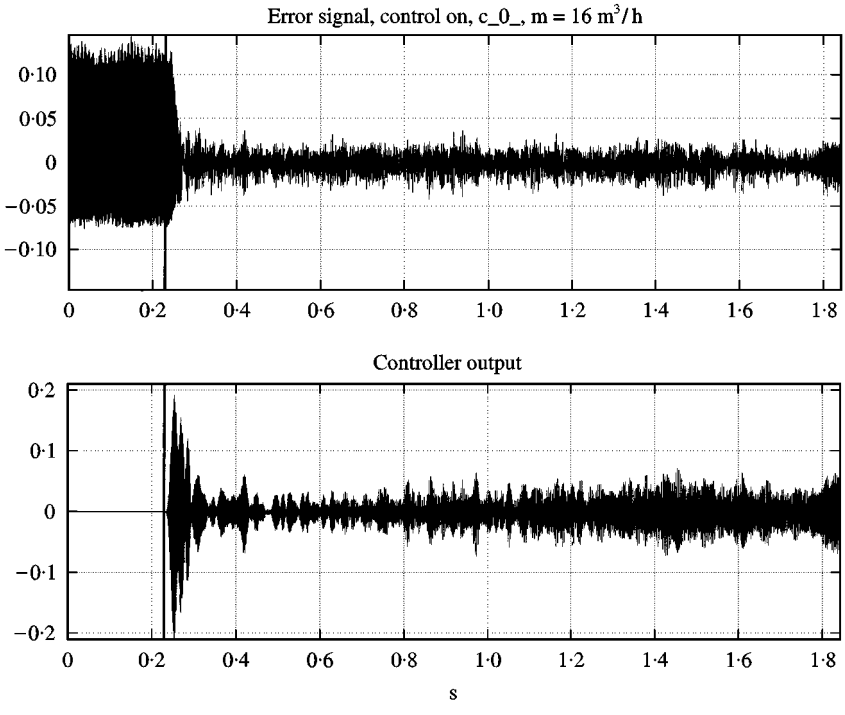

Figure 22. Error signal (upper plot) and controller action (lower plot). Air flow rate $\dot{V} = 16\ \mathrm{m}^3/\mathrm{h}$. Controller switch on.

typical for the controller acting on the source. Once the phenomena at the origin are reduced, only a relatively small amount of energy is needed to maintain control and the error level stays almost constant.

The influence of the controller on the system dynamics can also be analyzed by looking at the hot-film signal. The hot film, placed in the cavity, detects velocity fluctuations in the flow. Strong frequency components recorded in this way (see the upper plots in Figure 23 for the time domain and Figure 24 for the frequency domain) are associated with the vortices in the cavity. These structures are at the origin of the pressure oscillations. The hot-film signal becomes less coherent during control, although its amplitude does not change (see the lower plots in Figures 23 and 24). This suggests that the controller deorganizes the vortices. The energy of these structures is now distributed in the flow turbulence.

The present results agree with observations made by others (see, for example, Ziada [9], Ffowcs Williams and Zhao [10], Welsh *et al.* [11] or Blevins [22]). Ffowcs Williams proposes the following scenario. The shear layer response is initially linear and the shear flow is receptive to infinitesimal acoustic waves. A weak stimulus can thus amplify or attenuate the vortex shedding. In this way, the acoustic feedback from the second diaphragm helps to correlate the vortical structures. In the same way, an acoustic signal can also decorrelate the vortex formation process. This corresponds to the simple model devised to establish the two different control approaches. Active control can therefore be used to break the acoustic feedback (see references [9, 11]).

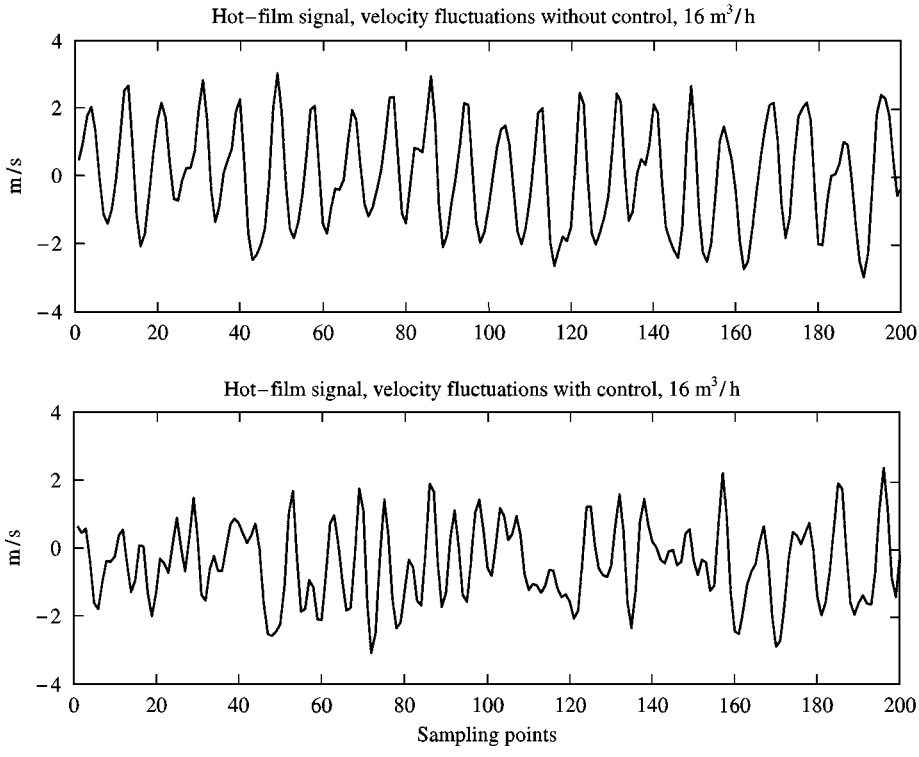

Figure 23. Hot-film signal, without (upper plot) and with control (lower plot), time domain. Air flow rate $\dot{V} = 16\,\mathrm{m}^3/\mathrm{h}$.

The acoustic power without and with control and the estimated acoustic power introduced into the system by the controller are displayed in Figure 25. In general, the controller works better than the anti-noise controller and the attenuations attained are more significant. The acoustic power used for accomplishing the control does not differ much from the anti-noise case. Only for very high flow rates (above 19 m^3/h) does the invested power grow rapidly. Again, the same problems as for the anti-noise controller appear. The algorithm cannot completely prevent the large peaks which dominate the controlled spectrum. The additionally invested power (with respect to the anti-noise algorithm) seems to be necessary to obtain the further reduction of the acoustic power (compare Figures 25 and 20).

5. CONCLUSION

Results described in this article show the potential for controlling aeroacoustic instabilities in a cold flow experimental set-up using two different approaches. The noise source controller clearly shows better performance than the anti-noise algorithm, suggesting that the acoustic driver unit signal acts at the noise source (the vortex shedding). This is confirmed by hot-wire anemometer measurements inside the cavity which show less coherent velocity fluctuations under controlled operation. The difference in the performance between the anti-noise and the noise

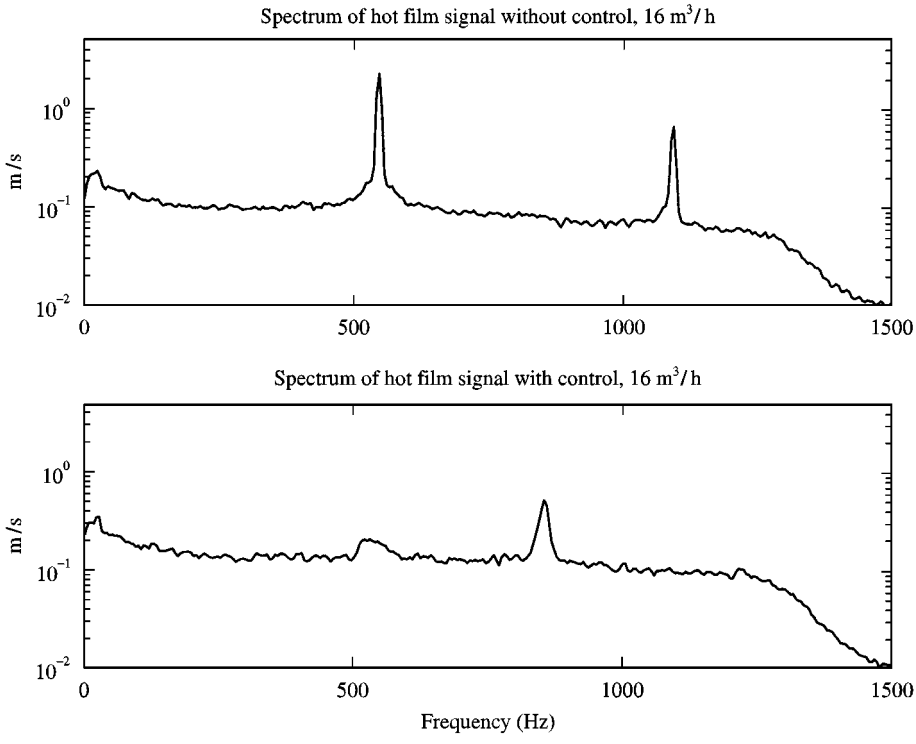

Figure 24. Hot-film signal, without (upper plot) and with control (lower plot), frequency domain. Air flow rate $\dot{V} = 16\ \mathrm{m}^3/\mathrm{h}$.

source controller is not due to a difference in the way the controller output acts on the system. In fact the anti-noise controller also acts at the noise source of the aeroacoustic instabilities. The difference is due to a more appropriate model of the real system used for the layout of the noise source algorithm.

The adaptive noise source controller is able to reduce the pressure oscillations by up to 40 dB. A stable state is reached after a short transition phase. The adaptive algorithms follow changes in the air flow rate and they adapt automatically to reduce the microphone signal.

The algorithms presented are less effective for frequency components of lower amplitude and broadband components of the spectrum. This is due to the feedback structure of the controller, which has to predict the primary noise at future sampling intervals. For broadband signals this is not possible.

The algorithms are also less effective for high mass flow rates. Although they are able to reduce the main peak by about 30 dB, a new high-frequency peak appears during control. This may be due to insufficient accuracy in the secondary path for high mass flow rates or to hydrodynamic phenomena. Further analysis is required to understand this effect.

The acoustic power needed for control is estimated to be generally less than 25% of the acoustic power in the system before control.

The choice of the sensors which can be used is restricted by two properties: first, the sensor which builds one part of the secondary path should be such that its

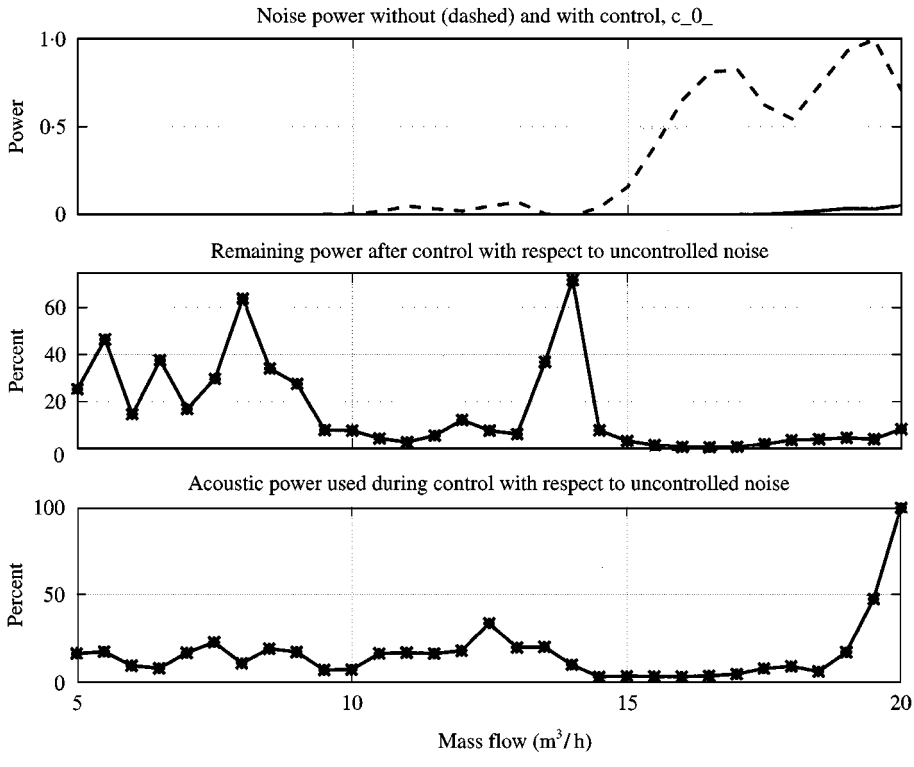

Figure 25. Comparison of the noise power with (——)/without (- - - -) control, normalized values (at the top), in percent (in the middle) and comparison *srd*/without control, in percent (at the bottom).

transfer function does not change too much during operation. Otherwise algorithms with on line identification of the secondary path will have to be used (in this respect, recent results obtained in the laboratory for the same experimental device are quite promising). Second, the signal used as input for the controller should be as deterministic and as correlated to the phenomenon to control as possible. Uncorrelated noise in the sensor signal degrades the controller performance.

ACKNOWLEDGMENT

This work was supported in part by the CNES. It is part of the research programme ASSM coordinated by CNES and ONERA.

REFERENCES

1. F. VUILLOT 1998 $3^{ème}$ *Colloque R&T*: *Ecoulement interne en propulsion solide*. CNES. Point sur les recherches relatives à la stabilité de fonctionnement du MPS P230 d'Ariane 5.
2. K. W. DOTSON, S. KOSHIGOE and K. K. PACE 1997 *Journal of Propulsion and Power* **13**, 197–206. Vortex shedding in a large solid rocket motor without inhibitors at the segmented interfaces.

3. H. Nomoto and F. E. C. Culick 1982 *Journal of Sound and Vibration* **84**, 247–252. An experimental investigation of pure tone generation by vortex shedding in a duct.
4. F. E. C. Culick and K. Magiawala 1979 *Journal of Sound and Vibration* **64**, 455–457. Excitation of acoustic modes in a chamber by vortex shedding.
5. R. Dunlap and R. S. Brown 1981 *AIAA Journal* **19**, 408–409. Exploratory experiments on acoustic oscillation driven by periodic vortex shedding.
6. X. Y. Huang and D. S. Weaver 1991 *Journal of Fluids and Structures* **5**, 207–219. On the active control of shear layer oscillations across a cavity in the presence of pipeline acoustic resonance.
7. G. Billoud, M. A. Galland, H. Can-Huynh and S. Candel 1991 *Journal of Intelligent Material Systems and Structure* **2**, 457–471. Adaptive active control of instabilities.
8. X. Y. Huang and D. S. Weaver 1994 *Journal of Sound and Vibration* **169**, 428–432. Control of flow-induced fin vibrations by anti-sound.
9. S. Ziada 1995 *Flow-Induced Vibration* (P. W. Bearman, editor), 579–591. Rotterdam: A. A. Balkema. Feedback control of globally unstable flows: impinging flows.
10. J. E. Ffowcs Williams and B. C. Zhao 1989 *Journal of Fluids and Structures* **3**, 115–122. The active control of vortex shedding.
11. M. C. Welsh, K. Hourigan, R. J. Alfredson and Pan Di Lin 1991 *International Conference on Flow Induced Vibrations. IMechE, May*. Active control of flow-excited acoustic resonance: higher order acoustic modes.
12. T. Poinsot, A. Trouvé, D. Veynante, S. Candel and E. Esposito 1987 *Journal of Fluid Mechanics* **177**, 265–292. Vortex driven acoustically coupled combustion instabilities.
13. R. S. Brown, R. Dunlap, S. W. Young and R. C. Waugh 1981 *Journal of Spacecraft and Rocket* **18**, 312–319. Vortex shedding as a source of acoustic energy in segmented solid rockets.
14. F. Vuillot 1995 *Journal of Propulsion and Power* **11**, 626–639. Vortex-shedding phenomena in solid rocket motors.
15. J. E. Rossiter 1964. *Technical Report and Memorandum No*. 3438, *Aeronautical Research Council*. Wind tunnel experiments on the flow over rectangular cavities at subsonic and transonic speeds.
16. D. Rockwell 1983 *AIAA Journal* **21**, 645–664. Oscillations of impinging shear layers.
17. R. C. Chanaud and A. Powell 1965 *Journal of the Acoustical Society of America* **37**, 902–911. Some experiments concerning the hole and ring tone.
18. S. E. Wright 1976 *Journal of Sound and Vibration* **45**, 165–223. The acoustic spectrum of axial flow machines.
19. B. Widrow and S. D. Stearns 1985. *Adaptive Signal Processing*. Englewood Cliffs, NJ: Prentice-Hall.
20. P. A. Nelson and S. J. Elliot 1992 *Active Control of Sound*. New York: Academic Press.
21. S. M. Kuo and D. R. Morgan 1996 *Active Noise Control Systems*. New York: John Wiley & Sons.
22. R. D. Blevins 1985 *Journal of Fluid Mechanics* **161**, 217–237. The effect of sound on vortex shedding from cylinders.